



**HAL**  
open science

## Three-dimensional numerical simulation of blood flow in mouse aortic arch around atherosclerotic plaques

Pauline Assemat, James A. Armitage, Karen K. Siu, Karla G. Contreras, Anthony M. Dart, Jaye P. Chin-Dusting, Kerry Hourigan

### ► To cite this version:

Pauline Assemat, James A. Armitage, Karen K. Siu, Karla G. Contreras, Anthony M. Dart, et al.. Three-dimensional numerical simulation of blood flow in mouse aortic arch around atherosclerotic plaques. *Applied Mathematical Modelling*, 2014, vol. 38 (n° 17-18), pp. 4175-4185. 10.1016/j.apm.2014.01.004 . hal-01785300

**HAL Id: hal-01785300**

**<https://hal.science/hal-01785300v1>**

Submitted on 4 May 2018

**HAL** is a multi-disciplinary open access archive for the deposit and dissemination of scientific research documents, whether they are published or not. The documents may come from teaching and research institutions in France or abroad, or from public or private research centers.

L'archive ouverte pluridisciplinaire **HAL**, est destinée au dépôt et à la diffusion de documents scientifiques de niveau recherche, publiés ou non, émanant des établissements d'enseignement et de recherche français ou étrangers, des laboratoires publics ou privés.



## Open Archive TOULOUSE Archive Ouverte (OATAO)


OATAO is an open access repository that collects the work of Toulouse researchers and makes it freely available over the web where possible.

This is an author-deposited version published in : <http://oatao.univ-toulouse.fr/>

Eprints ID : 19856

**To link to this article** : DOI:10.1016/j.apm.2014.01.004

URL : <http://dx.doi.org/10.1016/j.apm.2014.01.004>

**To cite this version** : Assemat, Pauline  and Armitage, James A. and Siu, Karen K. and Contreras, Karla G. and Dart, Anthony M. and Chin-Dusting, Jaye P. and Hourigan, Kerry *Three-dimensional numerical simulation of blood flow in mouse aortic arch around atherosclerotic plaques*. (2014) Applied Mathematical Modelling, vol. 38 (n° 17-18). pp. 4175-4185. ISSN 0307-904X

Any correspondence concerning this service should be sent to the repository administrator: [staff-oatao@listes-diff.inp-toulouse.fr](mailto:staff-oatao@listes-diff.inp-toulouse.fr)

# Three-dimensional numerical simulation of blood flow in mouse aortic arch around atherosclerotic plaques <sup>☆</sup>

Pauline Assemat <sup>a,\*</sup>, James A. Armitage <sup>b,c,d</sup>, Karen K. Siu <sup>e,f</sup>, Karla G. Contreras <sup>a</sup>, Anthony M. Dart <sup>d</sup>, Jaye P. Chin-Dusting <sup>d</sup>, Kerry Hourigan <sup>a</sup>

<sup>a</sup> Department of Mechanical and Aerospace Engineering & Division of Biological Engineering, Monash University, Victoria 3800, Australia

<sup>b</sup> School of Medicine (Optometry), Deakin University, Waurn Ponds, Victoria 3228, Australia

<sup>c</sup> Department of Anatomy and Developmental Biology, Monash University, Victoria 3800, Australia

<sup>d</sup> Baker IDI Heart and Diabetes Institute, 75 Commercial Rd, Melbourne, Victoria 3004, Australia

<sup>e</sup> Monash Biomedical Imaging, Monash University, Victoria 3800, Australia

<sup>f</sup> Australian Synchrotron, 800 Blackburn Rd, Clayton, Victoria 3168, Australia

---

## A B S T R A C T

Atherosclerosis is a progressive disease, involving the build-up of lipid streaks in artery walls, leading to plaques. Understanding the development of atherosclerosis and plaque vulnerability is critically important since plaque rupture can result in heart attack or stroke. Plaques can be divided into two distinct types: those likely to rupture (vulnerable) or less likely to rupture (stable). In the last decade, researchers have been interested in studying the influence of the mechanical effects (blood shear stress, pressure forces and structural stress) on the plaque formation, progression and rupture processes but no general agreement has been found. The purpose of the present work is to include more realistic conditions for the numerical calculations of the blood flow by implementing real geometries with plaques in the numerical model. Hemodynamical parameters are studied in both diseased and healthy configurations. The healthy configuration is obtained by removing numerically the plaques from three dimensional geometries obtained by micro-computed tomography. A new hemodynamical parameter is also introduced to relate the location of plaques to the characteristics of the flow in the healthy configuration.

### Keywords:

Atherosclerotic plaques  
Plaque progression  
Oscillating flow  
Mechanical effects  
Wall shear stress  
Pressure gradient

---

## 1. Introduction

Atherosclerosis is an inflammatory disease characterized by lipid and macrophages accumulation underneath the endothelium at the boundary of blood vessel walls. In addition to lipid deposition, atherosclerotic progression involves a complex process of monocyte infiltration, lipid oxidation, foam cell formation, smooth muscle cell migration and extracellular matrix production [1–3]. The lipid core is separated from the circulating blood by a fibrous cap composed of smooth muscle cells and extracellular matrix [2]. As plaques develop, they can cause luminal narrowing (reduction of the volume of the fluid

## Nomenclature

### Abbreviations

BCA	brachiocephalic artery
LCC	left common carotid artery
LDL	low density lipoproteins
LS	left subclavian artery
$\mu$ -CT	micro-computed tomography
OSI	oscillatory shear index
RRT	relative residence time
TAGP	time average gradient of pressure
TAWSS	time average wall shear stress
WSSG	wall shear stress gradient
WSS	wall shear stress

### Greek symbols

$\mu$	dynamic viscosity
$\rho$	density
$\tau_w$	instantaneous wall shear stress

part), or may undergo expansive remodeling to maintain lumen diameter [4,5]. Vulnerable plaques are prone to rupture, with disruption of the fibrous cap exposing the thrombogenic plaque core to the circulating blood [6]. Interactions between platelets and the lipid core can induce thrombus formation on the plaque surface, with possible consequences including vessel occlusion, myocardial infarction or stroke. While it is accepted that plaque vulnerability is influenced by fibrous cap thickness and the size of the lipid core [7], it also depends on biochemical factors, luminal remodeling and hemodynamic parameters for which no general agreement has been found [8,9].

Atherosclerotic plaques are found at particular sites in the arterial tree [10], with plaques commonly found on the inner curvatures of arteries and near bifurcations. This regional localization of atherosclerosis depends largely on hemodynamic factors such as wall shear stress (WSS) [2]. The distribution of the hemodynamic field depends on the geometrical patterns of the arteries, with low time averaged wall shear stress (TAWSS) commonly observed on inner curvatures of arteries and oscillatory TAWSS of low amplitude in regions of bifurcations [11]. This low WSS hypothesis for plaque formation and progression has been proposed by numerous groups [4,12–14] and has been related to the alteration of cholesterol transport [15]. In the regions of disturbed flow, the shape and direction of endothelial cells change and consequently does the permeability of the endothelial layer to external molecules [16,17]. In Liu et al. [18], the authors suggest that the concentration polarization of the low density lipoproteins (LDLs) and some specific aortic arch geometrical features are involved in the localization of the atherogenesis. Other hemodynamic factors are also thought to play a role in plaque development including the oscillatory shear index (OSI) [19–21], which quantifies the cyclic departure of the WSS vector from its predominant axial alignment, the wall shear stress gradient (WSSG) corresponding to spatial WSS variation [22,23], and the relative residence time (RRT) corresponding to a relative time spent by a particle at a specific site near the wall [24]. It is noticeable that the optimal hemodynamical parameter to relate subject specific physiological characteristics and plaque formation has not been agreed upon [25]. This uncertainty may be due to the fact that most of the studies that investigate the processes of early stage plaque formation consider healthy arteries and draw their conclusions assuming that plaques will grow in the most likely sites referenced in the literature. Thus, while it is largely agreed that atherosclerotic development occurs in regions of disturbed flow, the exact contributions of various hemodynamic parameters such as TAWSS, OSI, WSSG and RRT are still under debate.

In a similar way, the plaque growth process is poorly understood and the link with the mechanical effects not well identified. A limited number of recent studies [13,26–30] consider the details of processes of the growth of plaques after their initiation and, in particular, the influence of their presence on the blood flow. While researchers have attempted to correlate the plaque growth to hemodynamical factors, general conclusions cannot be drawn yet from these studies. Wong et al. [31] have suggested the potential implication of the structural stresses in plaque progression for a model carotid geometry, whereas Olgac et al. [28] propose the study of the LDL transport to understand the plaque expansion in the coronary arteries. In Olgac et al. [28], the authors numerically remove the plaques in order to compare the dynamics of the LDL transport and blood flow in effectively the same artery for healthy and disease state. In the present paper, a similar approach is used. A discussion is conducted on the validity and limitations of this approach. In addition, the present paper aims to develop a methodology to better understand the two questions of plaque formation and progression by investigating the hemodynamics of blood flow through the mouse aortic arch with and without plaques. Two mouse models are being studied: wild type C57/B6 mice (no plaque) and ApoE deficient mice (stable plaques). After the tissues have been fixed, the samples (mice aortic arch)

are imaged by micro-computed tomography ( $\mu$ -CT) using synchrotron X-ray beams; the resulting images are reconstructed to get the 3D geometries used for the numerical simulations. A high definition is clearly observed for each tissue (healthy wall, lipid core and fibrous cap) which can be reconstructed separately using segmentation tools. After the description of the experimental and numerical approach, validation and results will be presented.

## 2. Model description

### 2.1. Animal preparation

Animal models provide a key insight to understand atherosclerosis formation. In this study, the Apolipoprotein E knock-out (ApoE  $-/-$ ) mouse model, fed 12 weeks with a high fat diet (21% fat; 0.15% cholesterol), is used as a model for spontaneous atherosclerotic development [32]. While numerous physiological differences exist between mice and humans, ApoE  $-/-$  mice develop lesions in similar locations as human, suggesting that the arterial wall is affected in a similar manner by hemodynamical stresses [32]. Wild C57/B6 mice do not develop atherosclerosis and are used as controls in this investigation. The methodology presented in this paper use results obtained for two specific ApoE  $-/-$  and control mice. Mice were given a terminal dose of anesthetic and then transcardially perfused with heparinised saline to clear blood from the vasculature. Tissue was then perfusion fixed with Karnovsky's fluid (2% glutaraldehyde + 4% paraformaldehyde in 0.1 M phosphate buffer, pH 7.4). This procedure preserves vessel morphology in the native orientation. Tissues were then dissected, dehydrated through graded butanol and embedded in paraffin.

### 2.2. Imaging

Images of the mouse aortas have been obtained by micro-computed tomography using synchrotron X-ray beams (PSI, Swiss Light Synchrotron, Switzerland) and then reconstructed to derive the 3D geometries used for the numerical simulations (Fig. 1a). The  $\mu$ -CT data were acquired using monochromatic X-rays of 15 keV, and a CCD detector with X-ray converter and interchangeable objective lens to achieve pixel sizes in the range 2–6  $\mu$ m (as dictated by the sample size). The samples were imaged using a propagation distance (2–10 cm) to enhance the contrast of the lipid core/fibrous cap. The reconstruction employed the Paganin algorithm [33] using X-TRACT software developed at the CSIRO ([34], <http://www.ts-imaging.net/Services/AppInfo/X-TRACT.aspx>).

### 2.3. Numerical methods

#### 2.3.1. Geometry

The software X-TRACT provides two dimensional section images of the geometry which are then reconstructed in the 3D segmentation software AVIZO. The high spatial resolution of the images obtained by  $\mu$ -CT and the fine density contrast allowed us to differentiate the plaques from the artery walls. In consequence, the 3 dimensional geometries can be manually reconstructed using a region growing technique available in AVIZO: starting from a seed point within the region of interest (vessel wall or plaque), all connected voxels with intensity values within a predetermined range are associated with the corresponding material. An example of an obtained geometry can be seen in Fig. 1b. To obtain a geometry in the healthy configuration as described in Olgac et al. [28] (see Section 3.1 for the discussion), voxels belonging to the plaque are merged with

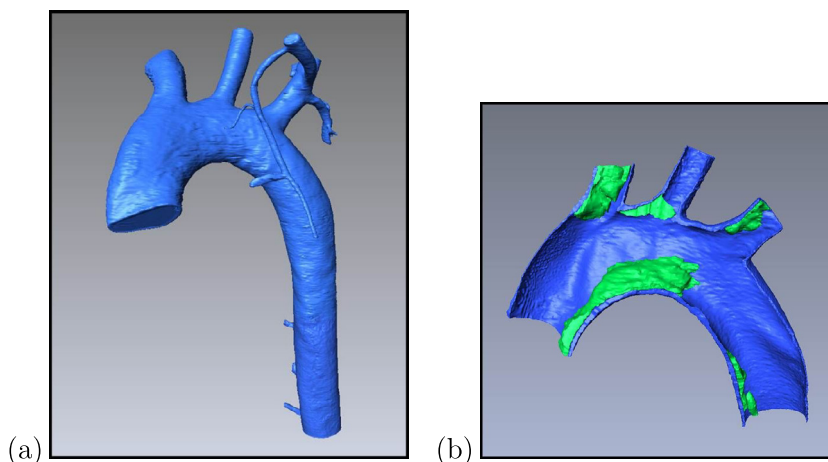


**Fig. 1.** (a) Reconstructed mouse aortic arch. (b) Half of the mouse aortic arch revealing the atherosclerotic plaque (green) on the inner part of the vessel wall. (For interpretation of the references to color in this figure legend, the reader is referred to the web version of this article.)

the lumen instead of being merged with the vessel wall as in the diseased case. To verify that the plaques were well defined in AVIZO, histochemical analyses were performed with Masson's Trichrome and the histochemical section compared with data obtained in Avizo (Fig. 2).

### 2.3.2. Mesh

Numerical meshing was conducted in the program ICEM CFD. The ends of the vessel were extended with an optimized length to ensure flow is fully developed in the region of interest (see next paragraph). A structured hexahedral mesh was produced using blocking and O-grid techniques. These techniques allow the mesh density to be tightly controlled, including the number and size of boundary layers, in addition to node distribution along the surface (Fig. 3). The complexity of the geometry due to the high curvature, the bifurcations and the presence of plaques makes the generation of the mesh a crucial and non-trivial step in the implementation of the numerical methods.

### 2.3.3. Numerical modeling

Numerical modeling was performed in ANSYS CFX. The Navier–Stokes equations were solved using the element based finite volume methods. Blood was considered Newtonian (the shear rates calculated are greater than  $150 \text{ s}^{-1}$ , a condition that make the Newtonian approximation relatively accurate [35]) with a density and dynamic viscosity of  $\rho = 1060 \text{ kg/m}^3$  and  $\mu = 0.0035 \text{ Pa}\cdot\text{s}$  [36]. The calculation of the time evolution of the solution was conducted for three cycles (0.45 s). Test calculations over a larger number of cycles have been performed to ensure the validation of the approach. The ends of the vessel were extended to ensure flow was fully developed in the region of interest. Since the main solution parameter of interest in the present paper is the WSS, extension length optimization was assessed by considering the maximum WSS and WSS at several points (local WSS) on the wall of the aortic arch. The curves relating the maximum WSS and the local WSS as a function of the extension length reach plateaus and the optimal length found was 1.5 times the equivalent inlet diameter, achieving a relative error of less than 0.1% with the maximum extension considered (3 equivalent inlet diameters). The mesh size and time step have been optimized using a relative convergence criteria of 0.2% (Fig. 4). The number of inflation layers in the vicinity of the wall insures the good description of the boundary layers. In the following, the time step is 0.001 s and the simulations are conducted on 1.5 million of cells meshes in both the cases of geometries with and without plaques.

### 2.3.4. Boundary conditions

The imposed boundary conditions in computational fluid dynamics simulations have a significant influence on the numerical results, and thus accurately defining the boundary conditions is crucial. In the present paper, the wall are considered rigid; while non-physical, this approximation has a weak influence of the calculation of time average hemodynamical factors [37]. When the walls are considered rigid (no slip boundary conditions), various kind of boundary conditions can be applied at the inlet and the outlets, provided the mass is conserved. The imposed boundary conditions can be associated with a scalar (pressure, flow rate) or with a vector field (velocity). When the boundary conditions are associated with the velocity, the question of the spatial distribution of this field is raised whereas when scalar values are used, the fully development of the flow has to be questioned. Combinations of different kind of boundary conditions for the inlet and the outlets are found in the literature. For the outlets, most of the references impose a percentage of the flow rate for each secondary branches, often taken as 15%, 8%, 7% for the brachiocephalic artery (BCA), left common carotid artery (LCC), left subclavian artery (LS) in mice [38–41] and of 5%, 5% and 5% in human [20,42]. For the descending aorta, the boundary conditions used are traction free boundary conditions [27,36,38], fraction of the flow rate [40], gradient-free normal velocity [41], pressure wave-forms [42], and Murray's law [36]. In the aortic arch region, only the work of Trachet et al. [36] discusses the effect of the outlet boundary conditions on the blood flow numerical calculations. In this paper, mice-specific flow rate have been compared to mice-averaged flow rate for the boundary conditions on the secondary branches. In addition, Murray's law have been implemented. It is shown that the use of average flow fractions for the numerical simulations instead of mice-specific data had limited effects. It is also shown that Murray's law can introduce some artifacts in the calculations. The authors

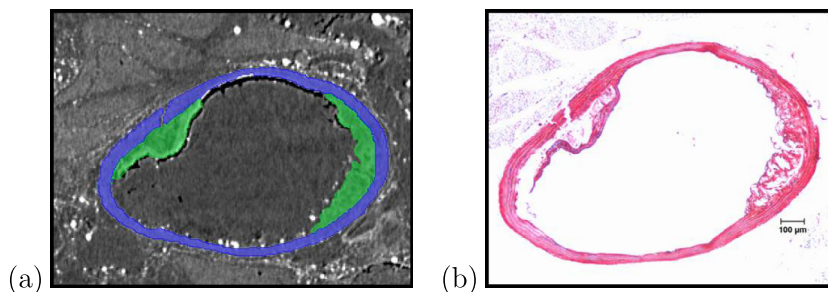


**Fig. 2.** Sections of the three-dimensional geometry. (a) Image obtained by  $\mu$ -CT, the blue color corresponds to the artery wall, the green to the plaque. (b) Histological analyse of the aortic arch. Sections were cut at  $5 \mu\text{m}$  through the entire aorta and stained with Masson's Trichrome in order to visualise the vascular structures and plaque. (For interpretation of the references to color in this figure legend, the reader is referred to the web version of this article.)

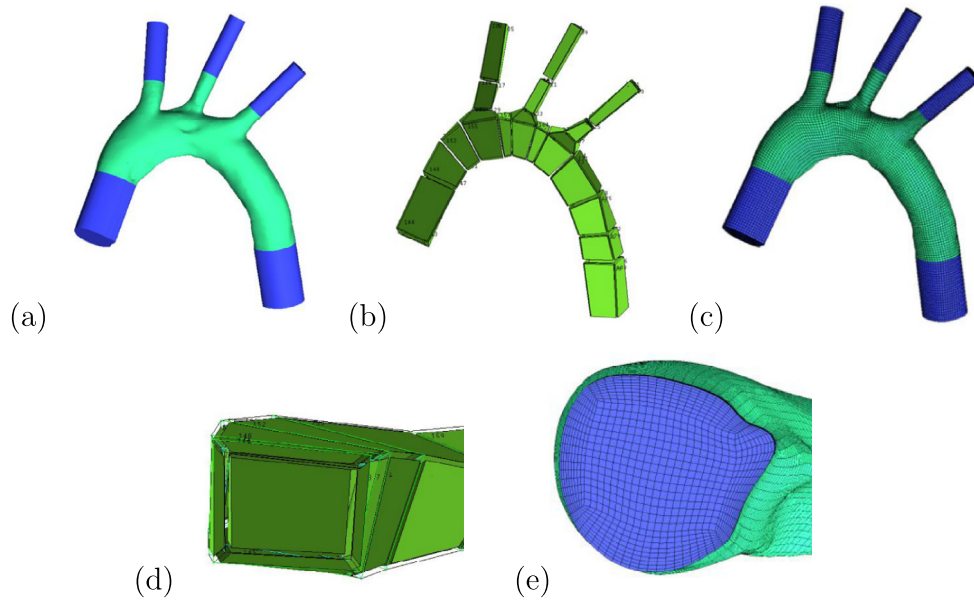


**Fig. 3.** Different steps used to build the mesh in ICEM CFD. (a) Extensions of the end of the vessel are indicated in blue. (b) Side view of the block distribution. (c) Final hexahedral mesh. (d) View of the block on the inlet. (e) View of the O-grid on the inlet. (For interpretation of the references to color in this figure legend, the reader is referred to the web version of this article.)

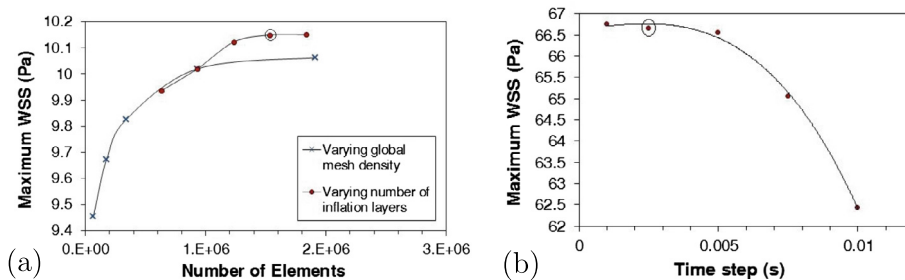


**Fig. 4.** (a) Convergence curve showing the maximum of WSS as a function of the number of mesh elements (b) Convergence curve showing the maximum of WSS as a function of time step.

conclude that a percentage of flow rate equal to 22.5%, 11.2%, 11.3% in the secondary branches can be suitable for computations in mice aortic arch. This result have been obtained on an average of 10 mice and will be used in the result section of the present article.

For the inlet, a similar variety of boundary conditions can be found in the literature such as time modulated volumetric flow rate [41,42] and physiological pressure waves [43]; however, most of the studies implement velocity profiles. Different velocity spatial profiles are found in the literature such as blunt profiles [20,27,39,40,44], parabolic profiles [36,45], Womersley profiles [38] and *in vivo* measured profiles [46,47,41]. Ideally, a subject-specific velocity profile should be used, but, in a study involving human carotids, Campbell et al. [48] concluded that a parabolic inlet profiles modulated in time were giving results in good correlation with subject-specific velocity profiles. In this study, blunt and Womersley profiles were shown to be less accurate. Similarly, Vandoormal et al. [41] conclude that whereas local differences in the hemodynamical parameters have been noticed when measured or idealized velocity inlet boundary conditions are used, the global WSS distribution is weakly affected. In addition, it is shown that mice-averaged inlet velocity profiles have a weak effect on the calculations compared to mice-specific profiles, a finding consistent with Trachet et al. work [36].

In the present study, Fourier series (order 16) were used to obtain time modulation of the flow rates from the data in Trachet et al. [36]. A heart rate of 400 beats per minute was assumed in agreement with the mean heart rate calculated on 10 mice in this article. In order to compare our results with the literature, the geometries obtained by  $\mu$ -CT have been slightly rescaled so that the inlet equivalent diameter (diameter of the circle whose surface is equal to inlet surface) is exactly 1.3 mm as referenced in [36,39,44].

### 2.3.5. Hemodynamical parameters

The hemodynamical parameters characterized in the present paper are based on the calculation of the instantaneous wall shear stress vector  $\tau_w$  with  $\tau_w = \mu \partial U / \partial n|_{wall}$  where  $U$  is the velocity field,  $n$  the outwards normal to the wall, and  $\mu$  the dynamic viscosity. The TAWSS, the OSI and the RRT are related to  $\tau_w$  through the following equations:

$$\text{TAWSS} = \frac{1}{T} \int_0^T |\tau_w| dt,$$

where  $T$  is a cardiac cycle period and  $t$  is time. As defined in the literature the others parameters are:

$$\text{OSI} = 0.5 \left( 1 - \frac{\left| \int_0^T \tau_w dt \right|}{\int_0^T |\tau_w| dt} \right),$$

$$\text{RRT} = \frac{1}{(1 - 2\text{OSI}) \text{TAWSS}}.$$

While TAWSS is directly obtained in ANSYS CFX, the two other parameters are calculated with in-house Matlab code using results from ANSYS CFX. Another parameter has been also investigated, the time average gradient of pressure (TAGP), defined by:

$$\text{TAGP} = \frac{1}{T} \int_0^T \nabla p dt,$$

where  $\nabla p$  is the gradient of pressure.

## 3. Results

### 3.1. Healthy versus diseased configuration: geometrical model

Before comparing the hemodynamical parameters in geometries with and without plaques, the validity of the healthy configuration obtained by removing numerically the plaque is discussed. The procedure consists in omitting the presence of the plaque during the segmentation process. This action can be achieved due to the high contrast of the images obtained with the synchrotron imaging technique. In these images, the wall and the plaque can be well differentiated (Fig. 5d). While this approach is quite easily implemented, the question of the accurate capture of the vessel wall remodeling is raised. The remodeling is defined by two aspects: the change in the shape of the vessel cross-sections and the vessel wall thickening [49]. Due to the *in vitro* nature of the experiments, the vessel's shape can be affected by the fixation of the tissue, the

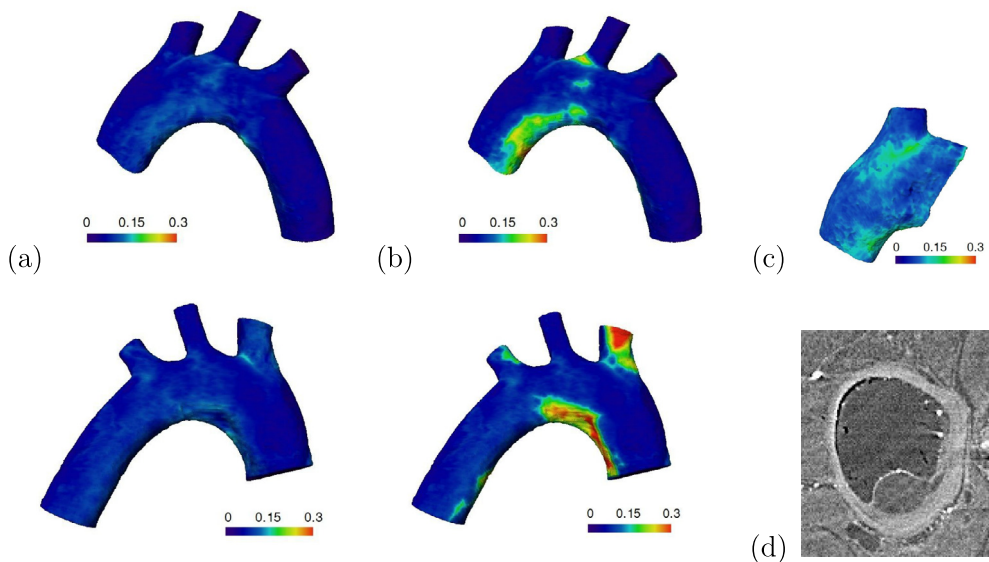


**Fig. 5.** Wall thickness in mm for the: (a) healthy configuration with the plaques numerically removed, (b) diseased configuration taking into account the plaques, (c) ascending aorta and BCA of control mice. (d) Cross section obtained by synchrotron imaging.



dissection procedure or small variation of the pressure during the injection of the fixative solution, and it is quite challenging to draw conclusions about this question using fixed tissues. However, it is expected these cross section shape changes to have a smaller effect on the flow than the plaques (smooth small amplitude obstacles versus sharp high amplitude obstacles).

Concerning the thickening of the artery wall due to the presence of plaques, Fig. 5 represents the thickness of the wall in the healthy (Fig. 5a) and diseased (Fig. 5b) configurations. Images have been obtained in the Avizo software. It can be seen on the figures that, in the healthy configuration, while variations are observed, the thickness remains relatively homogeneous when compared to the geometry where plaques have been taken into account. These variations can have different origins such as local shrinking due to the fixation of the tissue or errors in the segmentation process due to limited resolution of the edges of the vessel walls. Fig. 5c shows the wall thickness in a control mouse model (no plaque) and variations of similar amplitude can be observed. To conclude, even if some wall thickening could be present in the vicinity of plaques, its amplitude is of the order of the numerical error and so will be considered negligible in the following. This conclusion is limited to the present geometry and validation of the approach should be done for each subject-specific geometry. All together, it is considered that the geometry without plaques corresponds effectively to the geometry of the aortic arch of the same mice under an healthy condition.

### 3.2. Comparison with literature: implementation of two different boundary conditions

In order to compare our results with existing work, the two main types of outlet boundary conditions for mice aortic arches found in the literature are implemented. Those boundary conditions correspond to the cases of Trachet et al. [36] and Feintuch et al. [38] where the flow rate is split between the BCA, LCC, LS at 22.5%, 11.2%, 11.3% in the first case (case A) and 15%, 8%, 7% in the second (case B). In both cases, the conservation of mass is applied to impose the boundary condition in the descending aorta. The temporal modulation of the flow for inlet boundary condition is digitalized from Trachet et al. [36]. A plug profile is considered at the inlet of the geometry, however as the vessel is numerically extended, the flow can develop and a realistic profile is observed at the inlet of the actual geometry (green part of Fig. 3a). The systolic velocity profiles at the inlet and the outlets of the actual geometry are represented Fig. 6. The main difference between case A

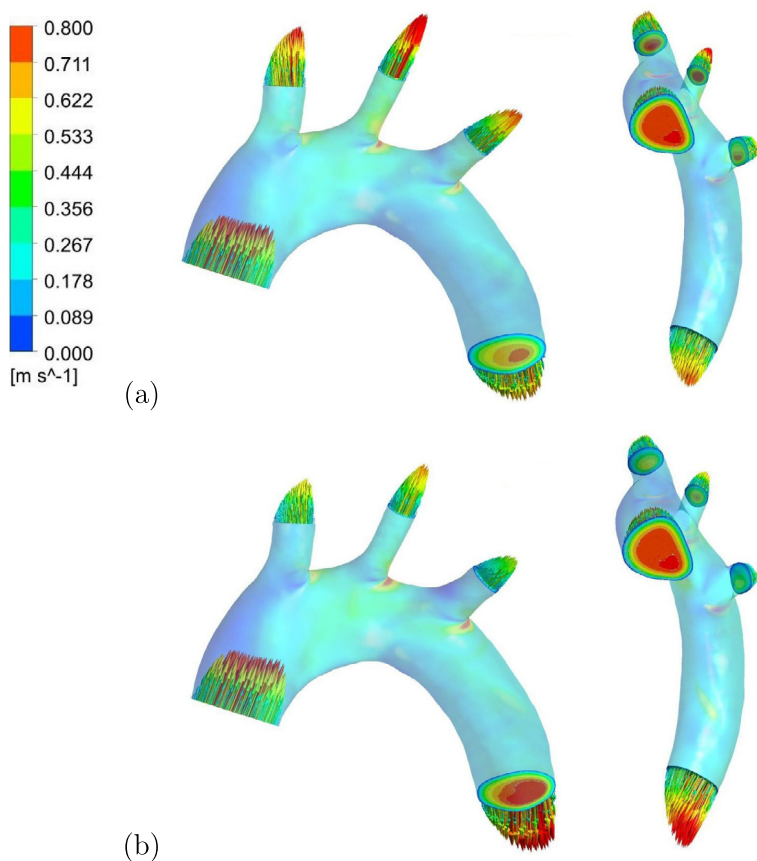


**Fig. 6.** Two views of the systole velocity field at the inlet and outlets considering: (a) 22.5%, 11.2%, 11.3% of the flow rate for the BCA, LCC, LS branches, values from Trachet et al. [36] boundary conditions, (b) 15%, 8%, 7% of the flow rate for the BCA, LCC, LS branches, values from Feintuch et al. [38]. Both isovalues and vector fields are represented. The transparent isocontours along the aortic arch wall correspond to the TAWSS represented on Fig. 7.

and case B is the amplitude of the maximum of velocity which, as expected, is found higher in case A due to a higher proportion flow rate going through the secondary branches (BCA, LCC, LS). It is noticeable that the spatial distribution of the velocity in the ascending aorta is similar to the *in vivo* measurements of Markl et al. [26] in human, with a local maximum of velocity shift towards the inner curvature of the vessel.

Fig. 7 shows the isocontours of TAWSS for cases A and B. The results are in quantitative and qualitative agreement with previous studies [36,38,39,41,44,50] conducted in mice aortic arches. Even if some slight quantitative variations can be observed due to geometry specificities (the order of magnitude is completely similar to the literature), the main features are preserved; local low shear stress zones are found at the front of ascending aorta, front of BCA, LCC, LS and in the inner curvature of the descending aorta (indicated by arrows on case B). As expected, the differences between case A and B are weak and only a slight modulation of the amplitudes of TAWSS are observed.

### 3.3. Comparison of hemodynamical parameters between healthy and diseased configuration

The TAWSS, OSI and RRT distributions for vessel without and with plaques are presented in Figs. 8 and 9. The presence of plaque was found to alter the TAWSS distribution on the vessel wall (Fig. 8c). The common effect of the plaque presence into the vessel is to increase locally the TAWSS, a phenomenon particularly amplified in the BCA and LCC on the plaques 2 and 3 (nomenclature defined in Fig. 8a). In these regions, the plaque causes significant luminal narrowing (maximum percentage blockage 27% in both cases), and the local TAWSS maxima are found to be correlated with the sites of maximal constriction. With ageing, plaques can undergo an erosion process and become vulnerable [8]. The local increase of TAWSS could be related to the erosion plaque process that leads to bursting, and if so, TAWSS could be used as a marker for vulnerability risk assessment. This hypothesis, however, needs to be confirmed by *in vivo* studies involving a long term follow-up of different subjects. In addition to the local TAWSS increase, the presence of plaques leads to a decrease of the TAWSS on the downstream side of the main aortic plaque (plaque 1). This region of low TAWSS could contribute to plaque progression, leading to enlargement of the existing atherosclerotic plaque. From the healthy configuration (Fig. 8b), it can be noticed that plaques arises in zones of low TAWSS; however, this assertion is relative and plaques can grow in areas where TAWSS is higher than in the surrounding regions (plaques 1,2,4). Considering the plaque birth position at the local minimum of TAWSS, its expansion seems to be directed through the zone where the wall shear stress increases or decreases the least. Concerning the OSI, results similar to those of Trachet et al. have been found [36,39]. In addition, while plaques do not grow in areas of minimum OSI (outer wall of descending aorta, downstream face of the secondary branches), there is no clear correlation between the plaque location and the amplitude of OSI. While plaques 2–5 are correlated with local increase of the OSI (clearly visible on plaque 5 on the LS branch Fig. 9 b), plaques 1 and 6 grow from each side of the local maximum of OSI in the inner curvature of the aortic arch. Furthermore, while local high RRT is related to plaques 1,3,5,6 (Fig. 9c), plaques 2 and 4 do not follow the same rule. To finish, areas of local low TAGP (Fig. 9d) gives a very good correlation with the plaques'

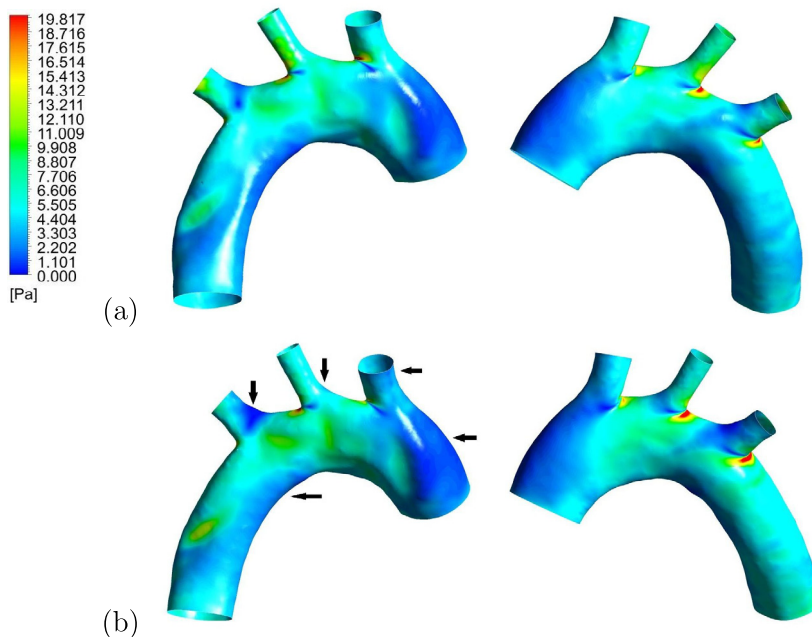


**Fig. 7.** Two views of isocontours of TAWSS considering: (a) 22.5%, 11.2%, 11.3% of the flow rate for the BCA, LCC, LS branches, values from Trachet et al. [36] boundary conditions, (b) 15%, 8%, 7% of the flow rate for the BCA, LCC, LS branches, values from Feintuch et al. [38].

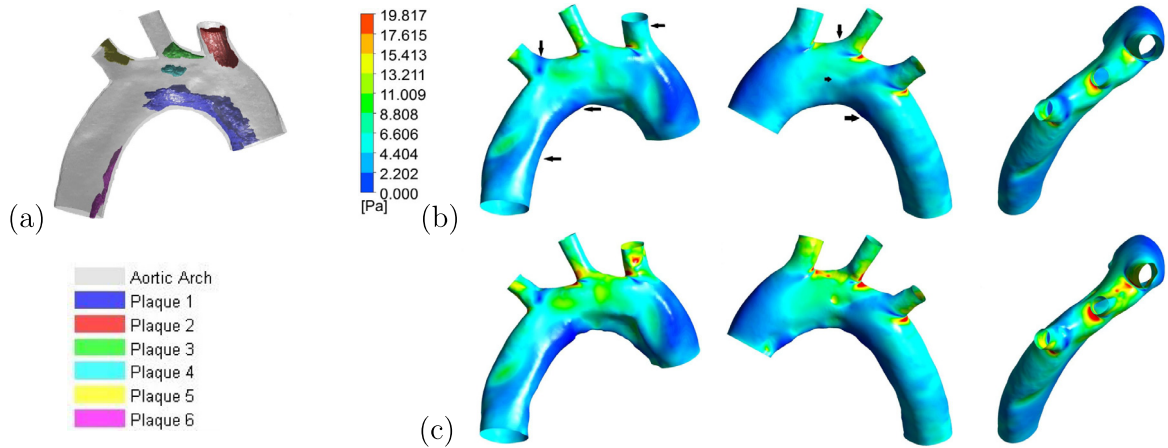


**Fig. 8.** (a) Location of plaques in the aortic arch with the corresponding nomenclature. Isocontours of TAWSS for (b) healthy (first row) and (c) diseased (second row) configurations under right, left and top views. Arrows indicate local minima of TAWSS in the healthy configuration related to plaque location.

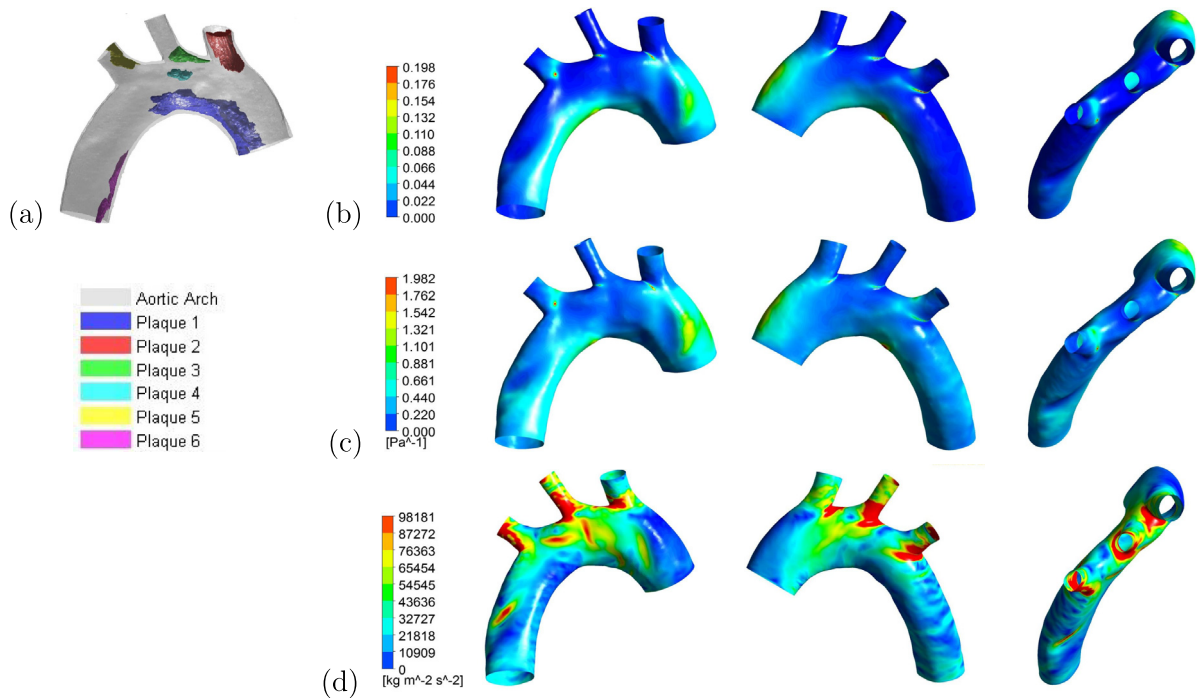


**Fig. 9.** (a) Location of plaques in the aortic arch with the corresponding nomenclature. Isocontours of (b) OSI (first row) and (c) RRT (second row) (d) TAGP (third row) under right, left and top views.

locations. This parameter gives a measure of the acceleration of the particles near the wall; therefore, it seems logical that plaques grow in quiescent areas in which fluid particles are weakly accelerated. This parameter has not been yet explored in the literature and further investigations are necessary to understand its possible involvement in the plaque growing process. In particular, a larger number of samples should be taken into account to check this hypothesis and draw additional conclusions using the methodology presented in this paper.

#### 4. Conclusion

This study is a first step in understanding the effect of hemodynamic parameters on plaque formation and development under realistic conditions. For the first time, a successful approach has been applied to the calculation of the blood flow in aortic arch geometries in the presence of plaques. It has been shown that the distribution of the flow rate in the secondary

branches have a weak impact on the hemodynamical parameters. The TAWSS results in the absence of plaque have been found quantitatively and qualitatively similar to those presented in the literature. The presence of plaque was found to increase TAWSS significantly, particularly in regions with large luminal narrowing, such as the brachiocephalic artery. Several studies suggest plaque rupture may be associated with high WSS [51,52], and hence the local maximum of WSS on the surface of the brachiocephalic plaque could contribute to plaque rupture; however, structural stresses are thought to play a more important role [53] in this process. Further investigations with the implementation of FSI is required to resolve this question under debate. The method of removing the plaque numerically to study the formation and the development of the plaque in the same artery has been discussed and predicts correctly the formation sites around local minimum of TAWSS. A new parameter, the TAGP, has been introduced and plaques are found to be located in areas where this parameter has a local minimum.

## Acknowledgments

The authors report no conflicts of interest in this work. The authors acknowledge financial support from the Australian Research Council, under Grant No. DP110100434. They acknowledge their collaborators Andrea Aprico, Karen Andrews from the Baker IDI Heart and Diabetes Institute, Stacey Hokke from Monash University for the preparation of the samples for Synchrotron imaging. They acknowledge also Jillian Hough, Gwenael Hannema, Kalgren Lai, three students involved in the project.

## References

- [1] P. Libby, Inflammation in atherosclerosis, *Nature* 420 (2002) 868–874.
- [2] Y.S. Chatzizisis, A.U. Coskun, M. Jonas, E.R. Edelman, C.L. Feldman, P.H. Stone, Role of endothelial shear stress in the natural history of coronary atherosclerosis and vascular remodeling, *J. Am. Coll. Cardiol.* 49 (25) (2007) 2379–2393.
- [3] O.M. Pello, C. Silvestre, M. De Pizzol, V. Andrs, A glimpse on the phenomenon of macrophage polarization during atherosclerosis, *Immunobiology* 216 (11) (2011) 1172–1176.
- [4] P.H. Stone, A.U. Coskun, S. Kinlay, J.J. Popma, M. Sonka, A. Wahle, Y. Yeghiazarians, C. Maynard, R.E. Kuntz, C.L. Feldman, Regions of low endothelial shear stress are the sites where coronary plaque progresses and vascular remodelling occurs in humans: an in vivo serial study, *Eur. Heart J.* 28 (6) (2007) 705–710.
- [5] A. Phinikaridou, N. Hua, T. Pham, J.A. Hamilton, Regions of low endothelial shear stress colocalize with positive vascular remodeling and atherosclerotic plaque disruption: an in vivo magnetic resonance imaging study, *Circ. Cardiovasc. Imaging* 6 (2) (2013) 302–310.
- [6] A.J. Reiningger, I. Bernlochner, S.M. Penz, C. Ravanat, P. Smethurst, R.W. Farndale, C. Gachet, R. Brandl, W. Siess, A 2-step mechanism of arterial thrombus formation induced by human atherosclerotic plaques, *J. Am. Coll. Cardiol.* 55 (11) (2010) 1147–1158.
- [7] T.G. Giannakopoulos, E.D. Avgerinos, K. Moulakakis, N.P. Kadoglou, O. Preza, A. Papapetrou, C. Papisideris, C.D. Liapis, Biomarkers for diagnosis of the vulnerable atherosclerotic plaque, *Interv. Cardiol.* 3 (2) (2011) 223–233.
- [8] S. Yl-Herttua, J.F. Bentzon, M. Daemen, E. Falk, H.M. Garcia-Garcia, J. Herrmann, I. Hoefler, J.W. Jukema, R. Krams, B.R. Kwak, N. Marx, M. Naruszewicz, A. Newby, G. Pasterkamp, P.W.J.C. Serruys, J. Waltenberger, C. Weber, L. Tokzoglu, Stabilisation of atherosclerotic plaques, *Thromb. Haemost.* 106 (1) (2011) 1–19.
- [9] P. Assemat, K. Hourigan, Evolution and rupture of vulnerable plaques: a review of mechanical effects, *ChronoPhysiol. Ther.* 3 (2013) 23–40.
- [10] M.S. Cocker, B. Mc Ardle, J.D. Spence, C. Lum, R.R. Hammond, D.C. Ongaro, M.A. McDonald, R.A. deKemp, J.-C. Tardif, R.S.B. Beanlands, Imaging atherosclerosis with hybrid [18F]fluorodeoxyglucose positron emission tomography/computed tomography imaging: what leonardo da vinci could not see, *J. Nucl. Cardiol.* 19 (6) (2012) 1211–1225.
- [11] C. Cheng, D. Tempel, R. van Haperen, A. van der Baan, F. Grosveld, M.J.A.P. Daemen, R. Krams, R. de Crom, Atherosclerotic lesion size and vulnerability are determined by fluid shear stress, *Circulation* 113 (23) (2006) 2744–2753.
- [12] C.M. Gibson, L. Diaz, K. Kandarpa, F.M. Sacks, R.C. Pasternak, T. Sandor, C. Feldman, P.H. Stone, Relation of vessel wall shear stress to atherosclerosis progression in human coronary arteries, *Arterioscler. Thromb. Vasc. Biol.* 13 (2) (1993) 310–315.
- [13] A. Harloff, A. Nubaumer, S. Bauer, A.F. Stalder, A. Frydrychowicz, C. Weiller, J. Hennig, M. Markl, In vivo assessment of wall shear stress in the atherosclerotic aorta using flow-sensitive 4d mri, *Magn. Reson. Med.* 63 (6) (2010) 1529–1536.
- [14] Y.S. Chatzizisis, A.B. Baker, G.K. Sukhova, K.C. Koskinas, M.I. Papafaklis, R. Beigel, M. Jonas, A.U. Coskun, B.V. Stone, C. Maynard, G.P. Shi, P. Libby, C.L. Feldman, E.R. Edelman, P.H. Stone, Augmented expression and activity of extracellular matrix-degrading enzymes in regions of low endothelial shear stress colocalize with coronary atheromata with thin fibrous caps in pigs, *Circulation* 123 (6) (2011) 621–630.
- [15] C.G. Caro, J.M. Fitz-Gerald, R.C. Schroter, Atheroma and arterial wall shear observation, correlation and proposal of a shear dependent mass transfer mechanism for atherogenesis, *Proc. R. Soc. London Ser. B Biol. Sci.* 177 (1046) (1971) 109–159.
- [16] D.K. Stangeby, C.R. Ethier, Computational analysis of coupled blood-wall arterial ldl transport, *J. Biomech. Eng.* 124 (1) (2002) 1.
- [17] R. Estrada, G.A. Giridharan, M.-D. Nguyen, S.D. Prabhu, P. Sethu, Microfluidic endothelial cell culture model to replicate disturbed flow conditions seen in atherosclerosis susceptible regions, *Biomicrofluidics* 5 (3) (2011) 032006.
- [18] X. Liu, F. Pu, Y. Fan, X. Deng, D. Li, S. Li, A numerical study on the flow of blood and the transport of ldl in the human aorta: the physiological significance of the helical flow in the aortic arch, *Am. J. Physiol. Heart Circ. Physiol.* 297 (2009) H163–H170.
- [19] D.N. Ku, D.P. Giddens, C.K. Zarins, S. Glagov, Pulsatile flow and atherosclerosis in the human carotid bifurcation. positive correlation between plaque location and low oscillating shear stress, *Arterioscler. Thromb. Vasc. Biol.* 5 (3) (1985) 293–302.
- [20] X. Liu, Y. Fan, X. Deng, F. Zhan, Effect of non-newtonian and pulsatile blood flow on mass transport in the human aorta, *J. Biomech.* 44 (6) (2011) 1123–1131.
- [21] T. Thim, A. Hrylc, A. Niemann, L. Drouet, H. B++tker, M. Hagensen, W. Kim, S. Thyse, W. Paaske, E. Falk, Wall shear stress and local plaque development in stenosed carotid arteries of hypercholesterolemic minipigs, *J. Cardiovasc. Dis. Res.* 3 (2) (2012) 76–83.
- [22] m. Lei, C. Kleinstreuer, G.A. Truskey, Numerical investigation and prediction of atherogenic sites in branching arteries, *Trans. ASME* 117 (1995) 350–357.
- [23] T.M. Farmakis, J.V. Soulis, G.D. Giannoglou, G.J. Zioupos, G.E. Louridas, Wall shear stress gradient topography in the normal left coronary arterial tree: possible implications for atherogenesis, *Curr. Med. Res. Opin.* 20 (5) (2004) 587–596.
- [24] H.A. Himgburg, D.M. Grzybowski, A.L. Hazel, J.A. LaMack, X. Li, M.H. Friedman, Spatial comparison between wall shear stress measures and porcine arterial endothelial permeability, *Am. J. Physiol. Heart Circ. Physiol.* 286 (5) (2004) H1916–H1922.
- [25] J. Knight, U. Olgac, S.C. Saur, D. Poulidakos, W. Marshall, P.C. Cattin, H. Alkadhi, V. Kurtcuoglu, Choosing the optimal wall shear parameter for the prediction of plaque location—a patient-specific computational study in human right coronary arteries, *Atherosclerosis* 211 (2) (2010) 445–450.

- [26] M. Markl, F. Wegent, T. Zech, S. Bauer, C. Strecker, M. Schumacher, C. Weiller, J. Hennig, A. Harloff, In vivo wall shear stress distribution in the carotid artery: effect of bifurcation geometry, internal carotid artery stenosis, and recanalization therapy, *Circ. Cardiovasc. Imaging* 3 (6) (2010) 647–655.
- [27] Y. Hoi, Y.-Q. Zhou, X. Zhang, R.M. Henkelman, D.A. Steinman, Correlation between local hemodynamics and lesion distribution in a novel aortic regurgitation murine model of atherosclerosis, *Ann. Biomed. Eng.* 39 (5) (2011) 1414–1422.
- [28] U. Olgac, J. Knight, D. Poulidakos, S.C. Saur, H. Alkadh, L.M. Desbiolles, P.C. Cattin, V. Kurtcuoglu, Computed high concentrations of low-density lipoprotein correlate with plaque locations in human coronary arteries, *J. Biomech.* 44 (13) (2011) 2466–2471.
- [29] H.S. Ryou, S. Kim, S.W. Kim, S.W. Cho, Construction of healthy arteries using computed tomography and virtual histology intravascular ultrasound, *J. Biomech.* 45 (9) (2012) 1612–1618.
- [30] J. Dong, K.K.L. Wong, J. Tu, Hemodynamics analysis of patient-specific carotid bifurcation: a cfd model of downstream peripheral vascular impedance, *Int. J. Numer. Methods Biomed. Eng.* 29 (4) (2013) 476–491.
- [31] K.K.L. Wong, P. Thavornpattanapong, S.C.P. Cheung, J.Y. Tu, Biomechanical investigation of pulsatile flow in a three-dimensional atherosclerotic carotid bifurcation model, *J. Mech. Med. Biol.* 13 (1) (2013) 1350001.
- [32] A.R. Bond, C.L. Jackson, The fat-fed apolipoprotein e knockout mouse brachiocephalic artery in the study of atherosclerotic plaque rupture, *J. Biomed. Biotechnol.* 2011 (2011) 1–10.
- [33] D. Paganin, S.C. Mayo, T.E. Gureyev, P.R. Miller, S.W. Wilkins, Simultaneous phase and amplitude extraction from a single defocused image of a homogeneous object, *J. Microsc.* 206 (2002) 33–40.
- [34] T.E. Gureyev, Y. Nesterets, D. Ternovski, D. Thompson, S. Wilkins, A.W. Stevenson, A. Sakellariou, J.A. Taylor, Toolbox for advanced x-ray image processing, *Proceedings SPIE* (2011). 81410B–14.
- [35] R.E.J. Wells, Shear rate dependence of the viscosity of whole blood and plasma, *Science* 133 (1961) 763–764.
- [36] B. Trachet, J. Bols, G. De Santis, S. Vandenberghe, B. Loeys, P. Segers, The impact of simplified boundary conditions and aortic arch inclusion on cfd simulations in the mouse aorta: a comparison with mouse-specific reference data, *J. Biomech. Eng.* 133 (12) (2011) 121006.
- [37] J. Lantz, J. Renner, M. Karlsson, Wall shear stress in a subject specific human aorta influence of fluid-structure interaction, *Int. J. Appl. Mech.* 03 (04) (2011) 759–778.
- [38] A. Feintuch, P. Ruengsakulrach, A. Lin, J. Zhang, Y.Q. Zhou, J. Bishop, L. Davidson, D. Courtman, F.S. Foster, D. Steinman, R. Henkelman, C. Ethier, Hemodynamics in the mouse aortic arch as assessed by mri, ultrasound, and numerical modeling, *Am. J. Physiol. Heart Circ. Physiol.* 292 (2007) H884–H892.
- [39] B. Trachet, A. Swillens, D. Van Loo, C. Casteleyn, A. De Paepe, B. Loeys, P. Segers, The influence of aortic dimensions on calculated wall shear stress in the mouse aortic arch, *Comput. Methods Biomech. Biomed. Eng.* 12 (5) (2009) 491–499.
- [40] H. Zhu, J. Zhang, J. Shih, D.S. Long, F. Lopez-Bertoni, J.R. Hagaman, N. Maeda, M.H. Friedman, Differences in aortic arch geometry, hemodynamics, and plaque patterns between c57bl/6 and 129/svev mice, *J. Biomech. Eng.* 131 (12) (2009) 121005.
- [41] M.A. Van Doormaal, A. Kazakidi, M. Wylezinska, A. Hunt, J.L. Tremoleda, A. Protti, Y. Bohraus, W. Gsell, P.D. Weinberg, C.R. Ethier, Haemodynamics in the mouse aortic arch computed from mri-derived velocities at the aortic root, *J. R. Soc. Interface* 9 (76) (2012) 2834–2844.
- [42] K.M. Tse, R. Chang, H.P. Lee, S.P. Lim, S.K. Venkatesh, P. Ho, A computational fluid dynamics study on geometrical influence of the aorta on haemodynamics, *Eur. J. Cardio Thorac. Surg.* 43 (4) (2012) 829–838.
- [43] P. Vasava, P. Jalali, M. Dabagh, P.J. Kolari, Finite element modelling of pulsatile blood flow in idealized model of human aortic arch: study of hypotension and hypertension, *Comput. Math. Methods Med.* 2012 (2012) 1–14.
- [44] Y. Huo, X. Guo, G.S. Kassab, The flow field along the entire length of mouse aorta and primary branches, *Ann. Biomed. Eng.* 36 (5) (2008) 685–699.
- [45] J. Renner, H. Nadali Najafabadi, D. Modin, T. Lne, M. Karlsson, Subject-specific aortic wall shear stress estimations using semi-automatic segmentation, *Clin. Physiol. Funct. Imaging* 32 (6) (2012) 481–491.
- [46] S. Jin, J. Oshinski, D.P. Giddens, Effects of wall motion and compliance on flow patterns in the ascending aorta, *J. Biomech. Eng.* 125 (3) (2003) 347–354.
- [47] C. Canstein, P. Cachot, A. Faust, A.F. Stalder, J. Bock, A. Frydrychowicz, J. Kffer, J. Hennig, M. Markl, 3d mr flow analysis in realistic rapid-prototyping model systems of the thoracic aorta: comparison with in vivo data and computational fluid dynamics in identical vessel geometries, *Magn. Reson. Med.* 59 (3) (2008) 535–546.
- [48] I.C. Campbell, D. Weiss, J.D. Suever, R. Virmani, A. Veneziani, R.P. Vito, J.N. Oshinski, W.R. Taylor, Biomechanical modeling and morphology analysis indicates plaque rupture due to mechanical failure unlikely in atherosclerosis-prone mice, *Am. J. Physiol. Heart Circ. Physiol.* 304 (2013) H473–H486.
- [49] M. Cilla, E. Pea, M.A. Martnez, D.J. Kelly, Comparison of the vulnerability risk for positive versus negative atheroma plaque morphology, *J. Biomech.* 46 (7) (2013) 1248–1254.
- [50] B. Vandeghinste, B. Trachet, M. Renard, C. Casteleyn, S. Staelens, B. Loeys, P. Segers, S. Vandenberghe, Replacing vascular corrosion casting by in vivo micro-ct imaging for building 3d cardiovascular models in mice, *Mol. Imaging Biol.* 13 (1) (2010) 78–86.
- [51] H.C. Groen, F.J.H. Gijzen, A. van der Lugt, M.S. Ferguson, T.S. Hatsukami, A.F.W. van der Steen, C. Yuan, J.J. Wentzel, Plaque rupture in the carotid artery is localized at the high shear stress region: a case report, *Stroke* 38 (8) (2007) 2379–2381.
- [52] D. Tang, Z. Teng, G. Canton, C. Yang, M. Ferguson, X. Huang, J. Zheng, P.K. Woodard, C. Yuan, Sites of rupture in human atherosclerotic carotid plaques are associated with high structural stresses: an in vivo mri-based 3d fluid-structure interaction study, *Stroke* 40 (10) (2009) 3258–3263.
- [53] U. Sadat, Z. Teng, J.H. Gillard, Biomechanical structural stresses of atherosclerotic plaques, *Expert Rev. Cardiovasc. Ther.* 8 (10) (2010) 1469–1481.